The Astrophysical Journal, 842:11 (10pp), 2017 June 10 https://doi.org/10.3847/1538-4357/aa7389
© 2017. The American Astronomical Society. All rights reserved.

Heating of Porous Icy Dust Aggregates

Sin-iti Sirono
Earth and Environmental Sciences, Nagoya University, Tikusa-ku, Furo-cho, Nagoya 464-8601, Japan
Received 2017 March 12; revised 2017 May 3; accepted 2017 May 14; published 2017 June 7

Abstract

At the beginning of planetary formation, highly porous dust aggregates are formed through coagulation of dust grains. Outside the snowline, the main component of an aggregate is H_2O ice. Because H_2O ice is formed in amorphous form, its thermal conductivity is extremely small. Therefore, the thermal conductivity of an icy dust aggregate is low. There is a possibility of heating inside an aggregate owing to the decay of radionuclides. It is shown that the temperature increases substantially inside an aggregate, leading to crystallization of amorphous ice. During the crystallization, the temperature further increases sufficiently to continue sintering. The mechanical properties of icy dust aggregates change, and the collisional evolution of dust aggregates is affected by the sintering.

Key words: planets and satellites: formation – protoplanetary disks

1. Introduction

Formation of dust aggregates inside a protoplanetary disk is the first step of planetary formation. Submicron-sized dust grains stick together because of surface cohesion. Successive collisions of dust grains promote the growth of dust aggregates. In the outer region of a protoplanetary disk, the main component of dust grains is H_2O ice because of low temperature. It has been shown that the porosity of dust aggregates is extremely high during their evolution (Kataoka et al. 2013). The high porosity is equivalent to the large cross sections, leading to the efficient growth of dust aggregates and planetesimal formation (Okuzumi et al. 2012). Gravitational instability of a layer composed of porous aggregates is also possible if the porosity is considerably high (Michikoshi & Kokubo 2016).

A dust grain is composed of ices and silicates. The silicate component of dust grains contains radionuclides such as ^{26}Al and ^{40}K, which are expected to contribute heating of asteroids (Ghosh & McSween 1998). If the size of an object is large, the generated heat is maintained inside the object and the temperature increases. The minimum size to melt H_2O ice inside an icy planetesimal is $\sim$10 km (Wakita & Sekiya 2011). Below this size, the heat conduction is effective, and the temperature increase is inadequate to melt H_2O ice.

H_2O ice in a dust grain is formed on the grain through surface reaction of OH and H_2 molecules (Oba et al. 2012). The formed ice is not crystalline, but amorphous (Oba et al. 2009). Kouchi et al. (1992) showed that the thermal conductivity of amorphous H_2O ice is $\sim 10^{-5}$ times lower than that of crystalline ice. This experimental result suggests that heating is possible even inside dust aggregates with a size of $\sim$10 m.

The heating can cause sintering of H_2O ice (Blackford 2007). Sintering is molecular transportation from a concave to a convex surface. Because a neck between adjacent grains is convex, it grows as sintering proceeds. The mechanical interactions between grains are greatly affected by sintering, and the collisional outcomes of sintered aggregates are totally different from those of nonsintered aggregates (Sirono & Ueno 2017). Further heating leads to melting of H_2O ice. If melting occurs, shrinkage of porous dust aggregates is expected.

There are heat conduction mechanisms other than that through the solid component of a dust aggregate. Gas molecules and radiation can contribute to heat transfer, particularly inside a porous medium (Krause et al. 2011). If one of these mechanisms is effective, temperature does not increase. In this study, we examine the contributions of the heat transfer mechanisms and determine the maximum temperature inside a porous dust aggregate. In Section 2, the thermal conductivities for various heat transfer mechanisms are compared. In Section 3, the temperature inside a porous dust aggregate is determined analytically and the results of numerical simulations are presented. The consequences of heating are discussed in Section 4. The conclusions are presented in Section 5.

2. Thermal Conductivities

A porous grain aggregate is composed of submicron-sized icy grains. The grains are connected to each other by surface cohesion, forming a porous structure (Figure 1). Here we assume a spherical aggregate of radius R with a packing fraction of ϕ, which is the volume fraction of the grains to the total volume of the aggregate. An aggregate can be cooled by several mechanisms (Figure 1). There are three important cooling mechanisms: conduction through grains, radiation inside pore spaces, and gas molecule transport. Conduction through grains is mainly determined by the thermal conductivity of H_2O ice, because its volume fraction is high (approximately 90% if we assume a silicate/ice mass ratio of 1:2). The thermal conductivity of amorphous H_2O ice $k_{\rm ice,a}$ and that of crystalline ice $k_{\rm ice,c}$ differ considerably (Kouchi et al. 1992). Both conductivities can be expressed as a function of temperature T as (Haruyama et al. 1993)

$$k_{\rm ice,a} = 7.1 \times 10^{-8}\left(\frac{T}{\rm K}\right) {\rm J\,m^{-1}\,K^{-1}},$$
$$\text{for amorphous } H_2O \text{ ice}, \quad (1)$$

$$k_{\rm ice,c} = 5.67 \times 10^{-1}\left(\frac{T}{\rm K}\right)^{-1} {\rm J\,m^{-1}\,K^{-1}},$$
$$\text{for crystalline } H_2O \text{ ice}. \quad (2)$$

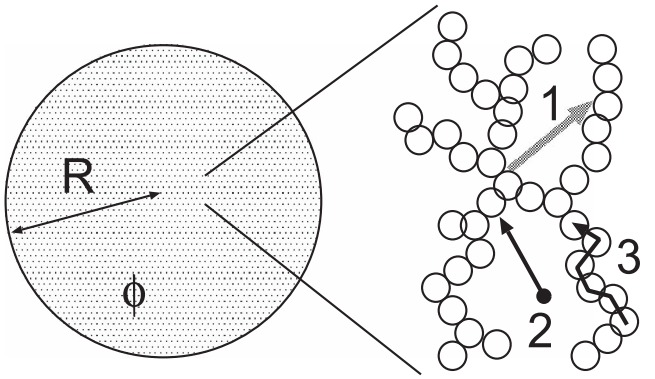

Figure 1. Schematic of heat transport mechanisms inside a porous dust aggregate of radius R and packing fraction ϕ: radiation (1), molecular transport (2), and conduction through grains (3).

The conductivity for amorphous ice $k_{\rm ice,a}$ is applicable under the temperature range between 30 and 100 K (Haruyama et al. 1993). We use this equation in the whole temperature range attained in this study (the maximum temperature is $\simeq$160 K). However, the duration of high temperature above 100 K is short, as shown later.

These conductivities are applicable for ices without porosity. Porosity (or packing fraction $\phi = 1 -$ porosity) dependence should be included for investigating the heat conduction inside a highly porous grain aggregate. Krause et al. (2011) experimentally determined the packing fraction dependence as $k(\phi) \propto A\exp(C\phi)$, where A and C are constants. This expression well approximates the experimental results in which the packing fraction ranges between 0.1 and 0.5. However, the range of the packing fraction, with which we are concerned, is considerably smaller than this range. Clearly, the expression is not applicable because it provides a finite conductivity even for $\phi = 0$. If we expand $k(\phi)$ to Taylor series, the first term should be zero. Consequently, the leading term is proportional to ϕ. Therefore, here we simply assume that the conductivities are expressed by $\phi k_{\rm ice,a}$ and $\phi k_{\rm ice,c}$ for porous amorphous and crystalline ice, respectively.

The thermal conductivity owing to radiation $k_{\rm rad}$ depends on the ambient gas temperature T_0 and the mean free path of radiation l as (Krause et al. 2011)

$$k_{\rm rad} = 4\sigma\epsilon T_0^3 l, \tag{3}$$

where σ is the Stefan–Boltzmann constant and ϵ is the emissivity. Here we adopt $\epsilon = 1$. Equation (3) does not change substantially even if $\epsilon < 1$ because l is equivalent to the inverse of the absorption coefficient, which is proportional to the emissivity $1/\epsilon$ by Kirchhoff's law. If we assume that the grains distribute randomly inside an aggregate, then l can be estimated from $l\pi r_{\rm g}^2 n = 1$, where $r_{\rm g}$ is the grain radius and $n = \phi/(4\pi r_{\rm g}^3/3)$ is the number density of grains inside an aggregate. This relation yields $l = 4r_{\rm g}/3\phi$.

The ambient gas temperature T_0 depends on the heliocentric distance a. We consider the distribution expressed by Chiang et al. (2001),

$$T_0(a) = 137\left(\frac{a}{1\ {\rm au}}\right)^{-3/7}. \tag{4}$$

As shown later, the main result does not depend on the temperature distribution.

Finally, the thermal conductivity by molecular transport $k_{\rm mol}$ is expressed as (Krause et al. 2011)

$$k_{\rm mol} = \frac{5}{6} n_{\rm gas} k_{\rm B} c l, \tag{5}$$

where $k_{\rm B}$ is the Boltzmann constant, c is the thermal velocity of gas, and $n_{\rm gas}$ is the number density of gas molecules at the midplane expressed by (Hayashi et al. 1985)

$$n_{\rm gas} = 3.6 \times 10^{20}\left(\frac{a}{1\ {\rm au}}\right)^{-11/4}\ {\rm m}^{-3}. \tag{6}$$

Figure 2 compares the heat conduction timescales normalized by Kepler frequency, expressed by $R^2\rho_{\rm av}c_{\rm av}/k_i t_{\rm Kep}$, where i is the label for conduction mechanisms, $t_{\rm Kep}$ is the Kepler frequency given by $2\pi\sqrt{a^3/GM}$, and the specific heat $c_{\rm av}$ of ice–silicate mixture is expressed as (Haruyama et al. 1993)

$$c_{\rm av} = c_{\rm av,0}T = 8.9(0.28 + 0.72\chi_{\rm ice})T \quad {\rm J\ kg^{-1}\ K^{-1}}, \tag{7}$$

where $\chi_{\rm ice}$ is the mass fraction of ice and assumed to be 2/3. This value is based on the silicate/gas ratio of 0.0043 and the ice/gas ratio of 0.0094, calculated from the solar elemental abundance (Miyake & Nakagawa 1993). The density of an aggregate $\rho_{\rm av}$ is expressed as

$$\rho_{\rm av} = \frac{\phi}{(1-\chi_{\rm ice})/\rho_{\rm sil} + \chi_{\rm ice}/\rho_{\rm ice}}, \tag{8}$$

where $\rho_{\rm ice} = 920\ {\rm kg\ m^{-3}}$ is the density of H_2O ice (Petrenko & Whitworth 2002) and $\rho_{\rm sil} = 3690\ {\rm kg\ m^{-3}}$ is the density of silicate represented by that of the mixture of H and L-chondrite (Neumann et al. 2012).

It should be noted that thermal conductivities and corresponding diffusivities ($k_i/\rho_{\rm av}c_{\rm av}$) have temperature dependencies. To compare the thermal diffusion timescales, we have to adopt an appropriate temperature because the temperature evolves from the initial temperature T_0. We adopt the temperature $T_{\rm eq}$ (shown later in Equation (15)) at which the crystallization of amorphous ice starts. The temperature evolution around $T_{\rm eq}$ determines the amount of crystallization and the degree of sintering.

In Figure 2, we adopt $R = 2 \times 10^2$ cm and $\phi = 10^{-3}$. It can be observed that the molecular diffusion is the most efficient mechanism in the inner region, and the radiation is the most efficient in the outer region, provided that H_2O ice is amorphous. The timescales are proportional to R^2. If we assume $R = 2 \times 10^1$ cm, the timescales decrease by a factor of 100. The heliocentric distance dependence is easily obtained from $t_{\rm Kep} \propto a^{3/2}$ except molecular transport, in which the dependence is $\propto a^{11/4-3/2}$ obtained from $n_{\rm gas} \propto a^{-11/4}$.

Dependence on ϕ differs between k_i. The timescales for amorphous and crystalline ice do not depend on ϕ because ρ and k are proportional to ϕ. Timescales for radiation and molecular diffusion are proportional to ϕ^{-1}, which is obtained from $l \propto \phi^{-1}$. Therefore, we can obtain timescales for different ϕ from Figure 2 by considering the ϕ dependencies.

We can conclude that the most important heat conduction mechanism is radiation if the ice is amorphous in a wide range of a protoplanetary nebula. If the ice becomes crystalline, the conduction through crystalline ice is the most efficient.

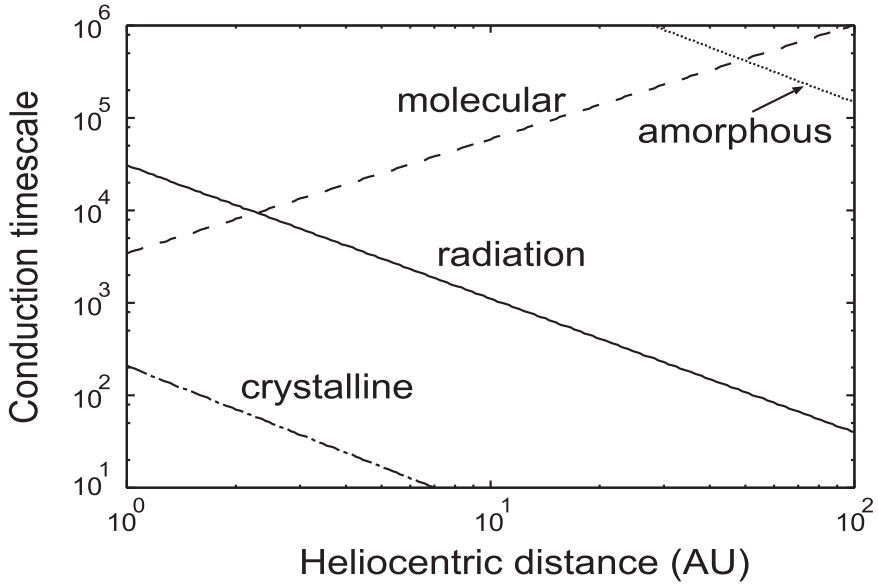

Figure 2. Heat conduction timescales for different mechanisms normalized by Kepler frequency. Each curve is labeled with corresponding conduction mechanisms. The size of an aggregate is 2×10^2 m.

3. Temperature inside a Porous Dust Aggregate

3.1. Analytical Calculation

Assuming a spherical aggregate with radius R, the temperature $T(r, t)$ at a distance of r from the center of an aggregate at time t is governed by the following heat conduction equation:

$$\rho_{\rm av} c_{\rm av} \frac{\partial T}{\partial t} = \frac{1}{r^2}\frac{\partial}{\partial r} r^2 k_{\rm total} \frac{\partial T}{\partial r} + Q, \tag{9}$$

where $k_{\rm total}$ is the sum of thermal conductivities consisting of three different mechanisms. However, as previously observed, the most effective mechanism is radiation.

If the fraction of crystallization ice ξ of H_2O ice is high, the conductivity is provided by that of crystalline ice. As ξ increases, the contribution of conduction through crystalline ice increases. We assume $k_{\rm total}$ as a function of ξ as

$$k_{\rm total} = k_{\rm rad} + \frac{k_{\rm c}}{2}[1 - \tanh((\xi_{\rm c} - \xi)/\Delta\xi)], \tag{10}$$

where $\xi_{\rm c}$ is the critical fraction of crystalline ice above which the crystalline part is mutually connected and the heat conduction through crystalline phase is possible. Because the heat is generated in the silicate core embedded inside H_2O ice, the crystallization proceeds from the inside of a grain. Thus, the surface of grains and connections between grains remain amorphous, and the heat conduction is not efficient, although crystallization proceeds substantially. Here we assume $\xi_{\rm c} = 0.9$ as a standard value. In Equation (10), $\Delta\xi$ is the transition width of ξ during the change of thermal conductivity and we assume $\Delta\xi = 0.01$.

Boundary conditions at the center and the surface of an aggregate are expressed as follows:

$$T = T_0 \quad \text{at} \quad r = R, \tag{11}$$

$$\frac{\partial T}{\partial r} = 0 \quad \text{at} \quad r = 0. \tag{12}$$

The heating rate Q consists of two terms, the decay of ^{26}Al radionuclides $Q_{\rm Al}$ and the crystallization of amorphous ice $Q_{\rm cry}$. ^{26}Al is contained in the silicate component with a number density of $f_{\rm Al} = 1.3 \times 10^{19}\,{\rm kg}^{-1}$ (Neumann et al. 2012). The decay constant of ^{26}Al is $\tau_{\rm Al} = 1.0 \times 10^6$ yr, and the energy released per one ^{26}Al atom $E_{\rm Al}$ is 6.4×10^{-13} J (Neumann et al. 2012). Combining these factors, we can obtain the heating rate inside an aggregate due to the decay of ^{26}Al as

$$Q_{\rm Al} = \frac{\rho_{\rm av}(1 - \chi_{\rm ice}) f_{\rm Al} E_{\rm Al}}{\tau_{\rm Al}} \exp(-t/\tau_{\rm Al}). \tag{13}$$

On the other hand, the heating rate of crystallization of amorphous ice is expressed as (Haruyama et al. 1993)

$$Q_{\rm cry} = \rho_{\rm av}\chi_{\rm ice} L \frac{d\xi}{dt} = \frac{\rho_{\rm av}\chi_{\rm ice} L(1 - \xi)}{A} \exp(-E_{\rm cry}/T), \tag{14}$$

where $A = 9.54 \times 10^{-14}$ s and $E_{\rm cry} = 7.41 \times 10^{-20}$ J (Schmitt et al. 1989). L is the latent heat of crystallization of amorphous H_2O ice. As a standard value, we adopt $L_0 = 2.55 \times 10^{-21}$ J(Ghormley 1968), which is the latent heat of crystallization of pure H_2O.

Because the timescale with which we are concerned is considerably shorter than the decay constant of ^{26}Al, we can neglect the last factor $\exp(-t/\tau_{\rm Al})$ in Equation (13).

$Q_{\rm Al}$ and $Q_{\rm cry}$ become equal at the temperature $T_{\rm eq}$, expressed by

$$T_{\rm eq} = \frac{E_{\rm cry}}{\log(\rho_{\rm av}\chi_{\rm ice}|L|/Q_{\rm Al}A)}. \tag{15}$$

If the temperature is less than $T_{\rm eq}$, $Q_{\rm cry}$ is negligible compared to $Q_{\rm Al}$ because of its exponential temperature dependence (Equation (14)). When $L > 0$, $Q_{\rm cry}$ steeply increases as T exceeds $T_{\rm eq}$. On the other hand, the temperature stays at $T = T_{\rm eq}$ when $L < 0$. In this case, heating by $Q_{\rm Al}$ and cooling by $Q_{\rm cry}$ balance at $T_{\rm eq}$. $T_{\rm eq}$ is 94 K for $L = L_0 = 2.55 \times 10^{-21}$ J.

If cooling by heat conduction and heating by crystallization are negligible, the temperature increases as $\rho_{\rm av} c_{\rm av,0} T dT/dt = Q_{\rm Al}$. Integrating this equation provides the time $\tau_{\rm eq}$ required to reach $T_{\rm eq}$

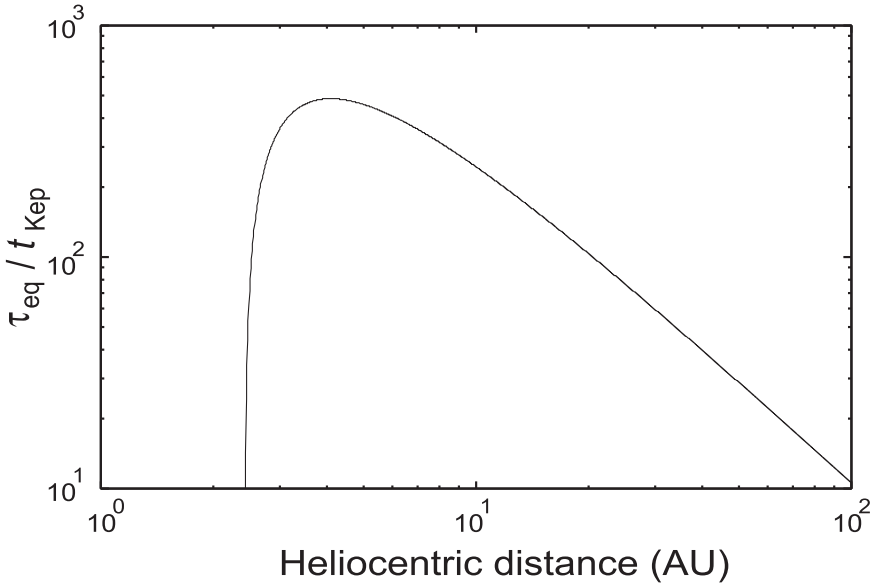

Figure 3. Time τ_{eq} required to reach T_{eq} normalized by Keplerian frequency as a function of heliocentric distance.

normalized by Keplerian frequency:

$$\frac{\tau_{eq}}{t_{Kep}} = \frac{(T_{eq}^2 - T_0^2)\rho_{av} c_{av,0}}{2Q_{Al} t_{Kep}}, \tag{16}$$

where $c_{av,0}$ is given by Equation (7). As shown in Figure 3, τ_{eq} becomes zero at $a = 2.4$ au, where the ambient temperature is T_{eq}. τ_{eq}/τ_{Kep} reaches the maximum of 4.8×10^2 at $a = 4.1$ au and decreases as a increases. From Figure 3, τ_{eq} is shorter than $100 t_{Kep}$ outside 20 au.

Because $Q \propto \phi$ and $k_{rad} \propto \phi^{-1}$ from Equation (9), the temperature distribution shall be the same if ϕR is a constant, provided that the radiation is dominant. In other words, the thermal evolution is not affected by decreasing ϕ by a factor of 10 and increasing R by a factor of 10 simultaneously. This is not the case if conduction through crystalline ice is dominant, because the thermal conductivity through ice is proportional to ϕ. In this case, the temperature evolution does not depend on ϕ. However, because the temperature evolution before crystallization determines the onset of crystallization, we expect that the overall temperature evolution is similar if ϕR is a constant.

The latent heat of crystallization expressed by $L_0 = 2.55 \times 10^{-21}$ J is for pure amorphous H_2O ice. Interstellar H_2O ices contain impurities such as CO, CO_2, CH_4, and NH_3 (Gibb et al. 2004). Kouchi & Sirono (2001) experimentally demonstrated that the latent heat is decreased by the addition of impurities because they take the latent heat of sublimation upon crystallization. This is the case if the impurities are homogeneously mixed with amorphous H_2O ice. The latent heat does not change if the impurities concentrate to form pure ice. We changed L from L_0 in the simulation for investigating the effect of impurities.

The temperature increases uniformly except near the surface for short timescales $t \ll \rho c_{av} R^2 / k_{rad}$. For long timescales $t \gg \rho c_{av} R^2 / k_{rad}$, the temperature distribution is approximately that of the steady state. Considering the temperature dependence of k_{rad}, we can calculate the steady-state temperature distribution as

$$T_{rad}(r) = \left(\frac{Q_{Al}}{6\sigma\epsilon l}(R^2 - r^2) + T_0^4 \right)^{1/4}, \tag{17}$$

if the radiation is the most effective. The temperature is close to T_0 if R is small, and it increases with $R^{1/2}$ if R is large.

The central temperature exceeds T_{eq} if the aggregate radius is larger than

$$R_c = \left(\frac{6\sigma\epsilon l}{Q_{Al}} (T_{eq}^4 - T_0^4) \right)^{1/2} = 1.8 \times 10^2 \left[1 - \left(\frac{T_0}{T_{eq}} \right)^4 \right]^{1/2} \left(\frac{\phi}{10^{-3}} \right)^{-1/2} \text{m}. \tag{18}$$

Aggregates larger than this size are heated above T_{eq} irrespective of R. Below this size, the maximum temperature is essentially determined by the ambient temperature T_0.

Figure 4 compares different temperatures. Two thick curves are the maximum central temperatures $T_{rad}(r = 0)$ for aggregate sizes of $R = 2 \times 10^2$ m and 1×10^2 m. The central temperature approaches these temperatures in the limit of $t = \infty$. Two dotted curves are the temperatures after $300 t_{Kep}$ and $30 t_{Kep}$ without cooling. The central temperature increases to that provided by the solid curve if the dotted curve exceeds the solid curve. It can be observed that the central temperature can reach to the solid curve outside 8 au after $300 t_{Kep}$.

An important temperature to be compared to $T_{rad}(r = 0)$ is T_{eq}, where the heating rates owing to the decay of ^{26}Al and crystallization of amorphous ice are equal. Above this temperature, heating owing to the release of the latent heat of crystallization dominates. It can be observed that if the aggregate size is larger than $R = 2 \times 10^2$ m, the central temperature exceeds T_{eq} irrespective of the heliocentric distance.

Through the analytical calculation presented earlier, we can predict whether heating occurs or not for a particular aggregate. Even if heating proceeds around the center, it is possible that

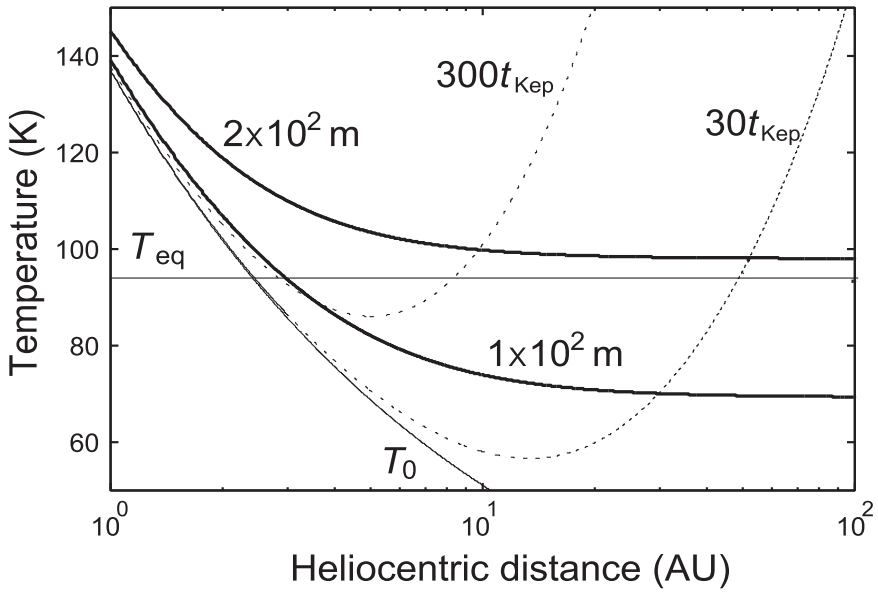

Figure 4. Comparison of temperatures analytically obtained. Thick curves labeled by 2×10^2 m and 1×10^2 m correspond for maximum central temperatures of aggregates with radii of $R = 2 \times 10^2$ m and $R = 1 \times 10^2$ m, respectively. The horizontal line is T_{eq}, and the lower thin curve is T_0. The dotted curves labeled $300t_{Kep}$ and $30t_{Kep}$ are the central temperatures at 300 and 30 Keplerian frequency, respectively, without any cooling.

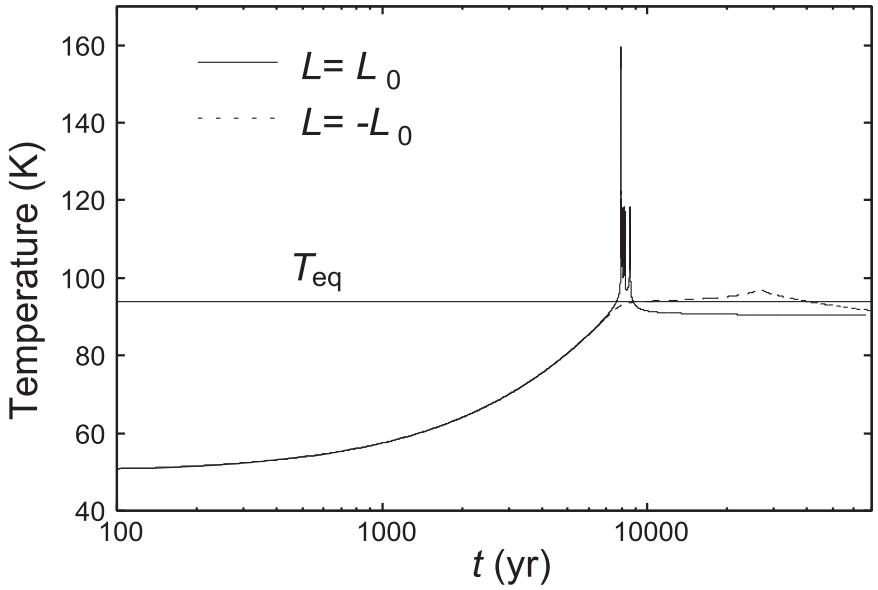

Figure 5. Evolution of the temperature at the center. Aggregate radius R is 10^3 m, and packing fraction ϕ is 10^{-3}. The initial temperature is 50 K. The solid curve is the evolution of an aggregate with $L = L_0$, and the dashed curve is $L = -L_0$. The horizontal line is $T_{eq} = 94$ K.

heating does not proceed around the surface. To understand the internal temperature distribution of an aggregate, numerical simulation of the thermal evolution of an aggregate is required.

3.2. Numerical Simulation Results

We numerically solved Equation (9) by an implicit scheme, with a spatial mesh width of $\Delta R/R = 10^{-4}$. Time step varies according to the heating rate by crystallization, because it changes by many orders of magnitude. The aggregate size R is varied between R $= 10^2$ and 3×10^5 m. The initial temperature is $T_0 = 50$ K, corresponding to the ambient temperature at $a = 10.5$ au in the model represented by Equation (4). The packing fraction is $\phi = 10^{-3}$. If R is larger than 2.5×10^5 m, H_2O ice melting occurs. Because shrinkage associated with melting is not included in this study, the simulation is applicable only for $R < 2.5 \times 10^5$ m.

Figure 5 shows the evolution of the temperature at the center for an $R = 10^3$ m aggregate with $L = L_0 = 2.55 \times 10^{-21}$ J and $L = -L_0 = -2.55 \times 10^{-21}$ J. As discussed in the previous subsection, the temperature gradually rises. When the temperature reaches T_{eq}, the two heating rates by the decay of ^{26}Al and by the crystallization of amorphous ice become comparable. Because the temperature continues to increase and the temperature dependence of crystallization is steep, the temperature drastically increases to a value greater than T_{eq} for an $L > 0$ aggregate. Then, the temperature quickly reaches to the peak temperature of $\simeq$160 K and decreases immediately. This is because the release of the latent heat of crystallization is

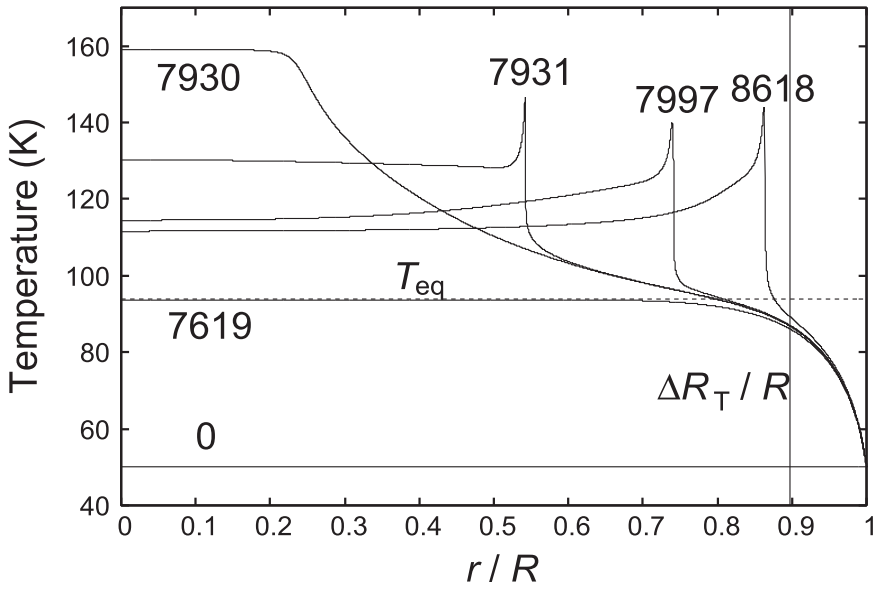

Figure 6. Evolution of the temperature distribution inside an aggregate of $R = 10^3$ m and $\phi = 10^{-3}$. The initial temperature is 50 K. The numbers associated with the curves are the elapsed time (in years) from the beginning. The vertical line at $\Delta R_T/R = 0.10$ is the thickness of the low-temperature region determined by Equation (19). The horizontal line is T_{eq}.

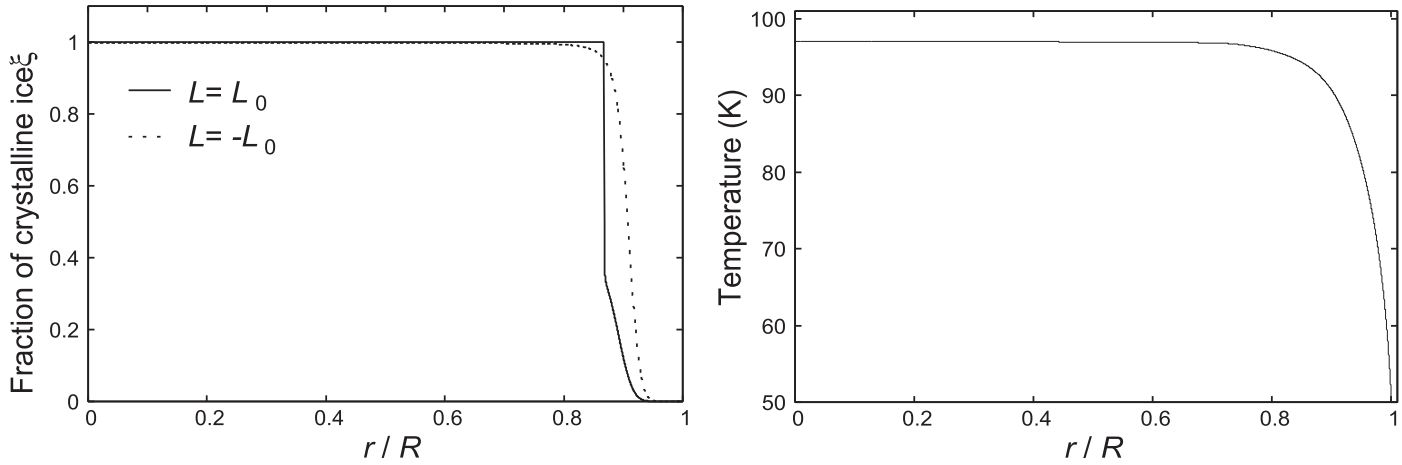

Figure 7. Left: distribution of the fraction of crystalline ice ξ at the end of simulation for $L = L_0$ (solid curve) and $L = -L_0$ (dashed curve). Right: temperature distribution when the temperature at the center of an aggregate with $L = -L_0$ reaches its peak.

completed at the center and the thermal conductivity changes from that of radiation to that of crystalline ice. The temperature oscillates around 110 K, as the boundary between crystalline and amorphous ice shifts outward. Finally, heating by Q_{Al} inside the aggregate and cooling by radiation through the low-temperature region around the surface balance, and the temperature remains constant.

Evolution of the temperature distribution inside the aggregate with $L = L_0$ is shown in Figure 6. At the beginning, the temperature uniformly increases except around the surface. When $t = 7619$ yr, the central temperature reaches T_{eq}. The temperature at the center reaches its peak of 160 K at $t = 7930$ yr. Then, the boundary between crystalline and amorphous ice expands to the surface. At the boundary, abrupt crystallization followed by cooling repeatedly proceeds, and the central temperature oscillates accordingly. When $t = 8618$ yr, heating by crystallization cannot exceed cooling from the surface, and therefore the crystallization stops. Then, the temperature gradually decreases from the surface. As observed previously, once the crystallization starts, the thermal evolution of an aggregate quickly proceeds. This is due to the strong temperature dependence of the crystallization rate (Equation (14)).

For an aggregate with $L = -L_0 < 0$, the evolution is totally different after reaching T_{eq}. The temperature gradually increases from $T_{eq} = 94$ K to the peak temperature of 97 K for $\simeq 2 \times 10^4$ yr (dashed line in Figure 5). Then, the temperature decreases gradually. The slight increase of temperature is due to the $1 - \xi$ dependence of Q_{cry}, which decreases as the crystallization proceeds. The fraction of crystalline ice ξ reaches $\xi_c = 0.9$ when the temperature at the center reaches its peak at $t = 2.7 \times 10^4$ yr. The left panel of Figure 7 shows the final distribution of ξ for $L = L_0$ and $L = -L_0$. Interestingly, both distributions are similar. Crystallization proceeds globally except around the surface in both cases. It can be seen that the thicknesses of low-temperature regions around the surface are the same for both $L = L_0$ and $L = -L_0$ cases (compare Figure 6 and the left panel of Figure 7).

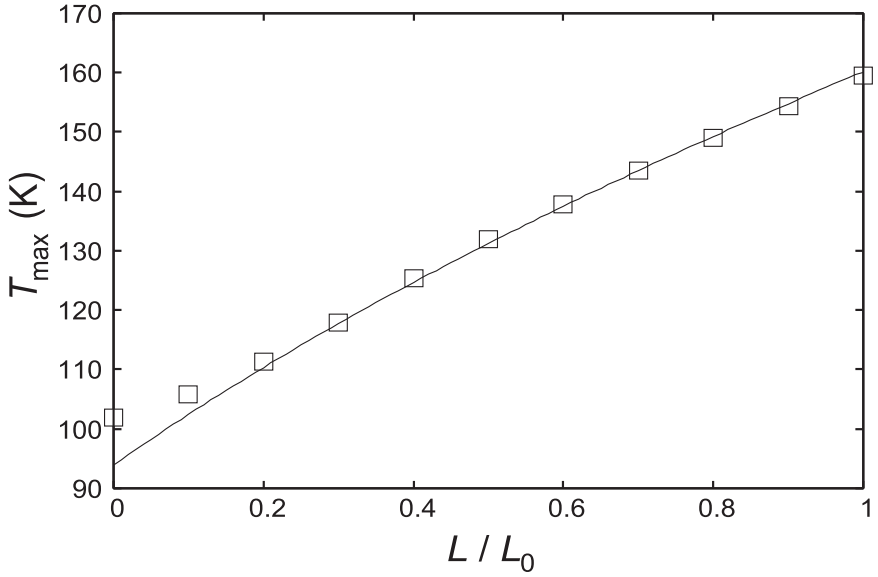

Figure 8. Maximum temperature attained in an aggregate of $R = 10^3$ m. The solid curve is expressed by Equation (21).

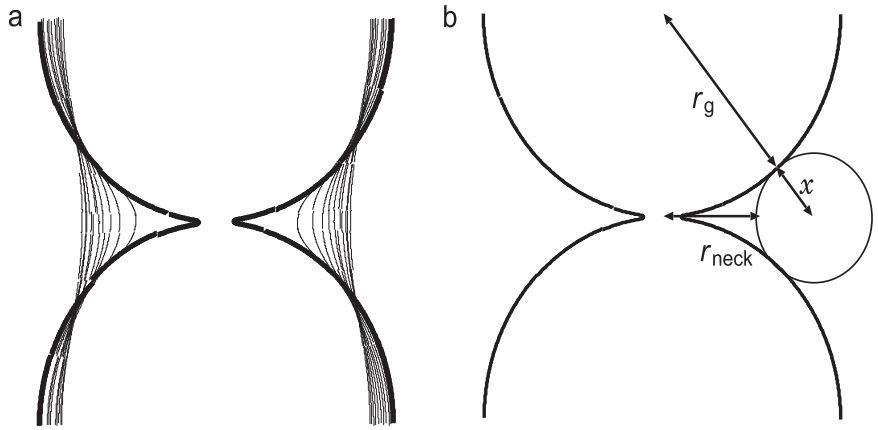

Figure 9. (a) Schematic of the evolution of the shape of a neck as sintering proceeds. The thick curve is the initial surface profile. Thin curves are the profiles as time proceeds. (b) The neck profile is approximated by a circle with a radius x smoothly connected to the spherical grains of radius r_g.

The temperature around the surface is low throughout the simulation because the surface temperature is fixed to 50 K. Ice around the surface is still amorphous, and the dominant cooling mechanism is radiation in this region. The thickness of this low-temperature region ΔR_T can be estimated by

$$\Delta R_T = \sqrt{\frac{k_{rad}(T_{eq})}{\rho_{av} c_{av}} \tau_{eq}}, \tag{19}$$

where τ_{eq} is expressed by Equation (16). If we assume $\phi = 10^{-3}$, $\Delta R_T = 1.0 \times 10^2$ m. In Figure 6, $\Delta R_T / R$ is shown as the vertical line. Equation (19) well estimates the thickness of the low-temperature region. Because of $k_{rad} \propto \phi^{-1}$, $\rho_{av} \propto \phi$, and $Q_{Al} \propto \phi$, the thickness ΔR_T is proportional to ϕ^{-1}.

Impurities such as CO escape from amorphous H_2O ice upon crystallization. Simultaneously, the impurity molecule takes the latent heat of sublimation if its condensation temperature is lower than the temperature of the ice. Thus, the maximum temperature shown in Figure 5 depends on L. If cooling by conduction is negligible, the maximum temperature by crystallization can be obtained by integrating (see Equations (9) and (14))

$$\int_{T=T_{eq}}^{T=T_{max}} \rho_{av} c_{av,0} T dT = \int_{\xi=0}^{\xi=1} \rho_{av} \chi_{ice} L d\xi \tag{20}$$

as

$$T_{max} = \sqrt{2 \frac{\chi_{ice} L}{c_{av,0}} + T_{eq}^2}. \tag{21}$$

Figure 8 compares the temperature estimated by Equation (21) and the maximum temperature at the center of an $R = 10^3$ m aggregate, obtained from numerical simulation. It can be observed that Equation (21) well represents the numerical results, except around $L \sim 0$. This is because Equation (21) does not contain the contribution from the heating owing to the decay of ^{26}Al, leading to an underestimate of the maximum temperature expressed by Equation (21). It should be noted that Equation (21) does not depend on the ambient gas temperature T_0.

From Figure 8, the maximum temperature varies between 160 and 100 K depending on L. At this temperature range,

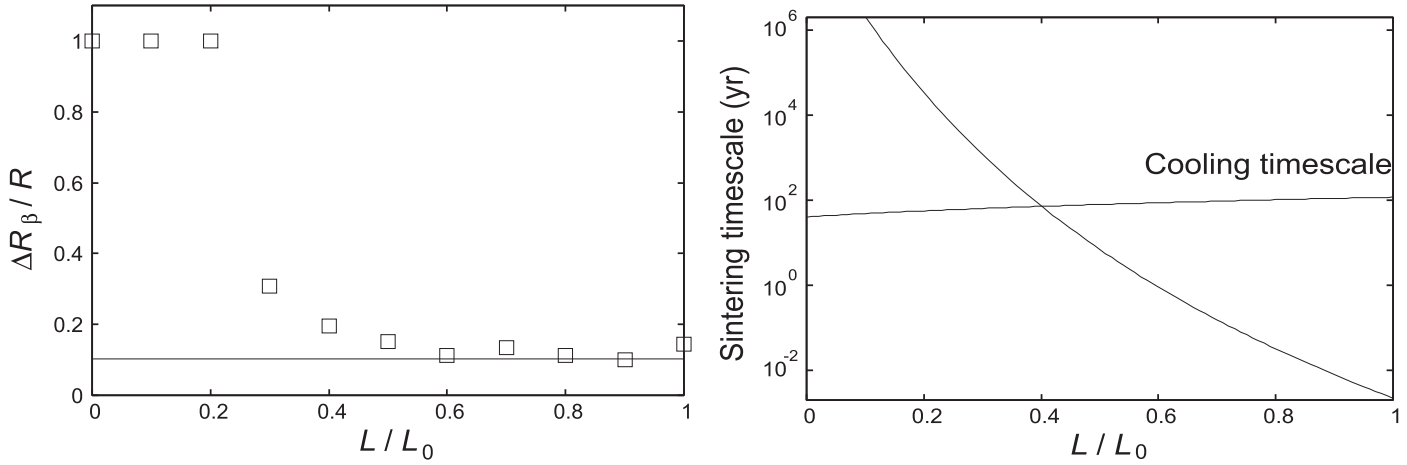

Figure 10. Left: location of the boundary $\Delta R_\beta/R$ below which the sintering degree $\beta = r_{\rm neck}/r_{\rm g}$ is larger than 0.5 as a function of latent heat of crystallization L/L_0. The aggregate radius is 10^3 m. The horizontal lines denote the thickness of the low-temperature region expressed by Equation (19). Right: sintering timescale defined by Equation (25) as a function of L/L_0. The horizontal curve is the cooling timescale of an aggregate with a radius of 10^3 m.

sintering can proceed inside an aggregate. Sintering increases the mechanical strengths of an aggregate and would affect the collisional evolution of an aggregate (Sirono & Ueno 2017). Simultaneously, the increase of the strengths also affects the porosity evolution of an aggregate (Kataoka et al. 2013).

The degree of sintering is determined by the radius of a neck $r_{\rm neck}$ connecting the adjacent grains. The radius grows by molecular transport from the main part of an icy grain (Figure 9(a)). The growth rate depends on the curvature of neck Γ, which is the sum of two principal radii of curvature. One is the neck radius $r_{\rm neck}$. The other one is the radius of curvature along the direction of connecting two grain centers (Figure 9(b)). If we approximate the shape of a neck by a circle connecting two grains (Figure 9(b)), the radius of the circle x is expressed by

$$x = \frac{r_{\rm neck}^2}{2(r_{\rm g} - r_{\rm neck})}. \tag{22}$$

Using this formula as the radius of curvature, the curvature Γ can be written as

$$\begin{aligned}\Gamma &= -\frac{2(r_{\rm g} - r_{\rm neck})}{r_{\rm neck}^2} + \frac{1}{r_{\rm neck}} \\ &= -\frac{2r_{\rm g} - 3r_{\rm neck}}{r_{\rm neck}^2},\end{aligned} \tag{23}$$

where the minus sign comes from the concave shape of the surface along the direction of connecting two grain centers. Along the perpendicular direction ($r_{\rm neck}$), the surface is convex and the sign is positive.

The degree of sintering can be computed by integrating (Sirono 2011)

$$\begin{aligned}\frac{dr_{\rm neck}}{dt} &= \frac{P_{\rm H_2O}(T)\gamma\Omega^2}{\sqrt{2\pi m_{\rm H_2O}k^3T^3}}(\Gamma_{\rm av} - \Gamma) \\ &\simeq \frac{P_{\rm H_2O}(T)\gamma\Omega^2}{\sqrt{2\pi m_{\rm H_2O}k^3T^3}}\frac{2r_{\rm g} - 3r_{\rm neck}}{r_{\rm neck}^2},\end{aligned} \tag{24}$$

where $P_{\rm H_2O}(T) = \exp(28.55 - 6070/T)$ Pa, (T in kelvin; Bauer et al. 1997) is the equilibrium vapor pressure of H_2O, $\gamma = 0.069$ J m^{-2} is the surface energy of H_2O ice (Petrenko & Whitworth 2002), $\Omega = 3.25 \times 10^{-29}$ m^3 is the molecular volume of H_2O, $m_{\rm H_2O} = 3.0 \times 10^{-26}$ kg is the molecular mass of H_2O, and $\Gamma_{\rm av}$ is the curvature averaged over the entire surface. Here we neglect $\Gamma_{\rm av}$ because $\Gamma \gg \Gamma_{\rm av}$ except at the last stage of sintering. It should be noted that $dr_{\rm neck}/dt = 0$ when $r_{\rm neck} = 2/3$, at which the growth of a neck stops. The numerical simulations show that the final neck radius is $\simeq 0.8 r_{\rm g}$ (Sirono 2011).

Figure 10 shows the thickness of less sintered zone ΔR_β, inside which the degree of sintering $\beta = r_{\rm neck}/r_{\rm g}$ is less than 0.5, as a function of the latent heat of crystallization L/L_0. The threshold of 0.5 has been observed (Sirono & Ueno 2017), above which the collision between porous sintered aggregates is affected by sintering. It can be observed that the thickness is well explained by the thickness of the low-temperature zone expressed by Equation (19). The thickness increases at $L/L_0 = 0.4$. This is because the maximum temperature is inadequate for sintering to proceed for small L. This transition can be explained in terms of the sintering timescale. Based on the growth rate of a neck expressed by Equation (24), we can estimate the timescale required for sintering as

$$\tau_{\rm sint}(T) = \frac{r_{\rm g}^2\sqrt{2\pi m_{\rm H_2O}k^3T^3}}{P_{\rm H_2O}(T)\gamma\Omega^2}. \tag{25}$$

Adopting $T_{\rm max}$ of Equation (21) as T in Equation (25), we can obtain the timescale for sintering as a function of L/L_0, as shown in the right panel of Figure 10. The horizontal curve is the cooling timescale of an aggregate of $R = 10^3$ m. If the sintering timescale is less than the cooling timescale $R^2\rho_{\rm av}c_{\rm av,0}T_{\rm max}/k_{\rm rad}$, sintering can proceed. It can be observed that the intersections between the sintering and cooling timescales well explain the transition of ΔR_β.

4. Discussion

4.1. Evolution of an Icy Dust Aggregate

Icy dust aggregates grow through sticking collisions of icy dust grains. As an aggregate grows, the timescale of the gas drag increases. When the gas drag timescale and the Kepler frequency are comparable (Stokes number St is unity), an aggregate quickly infalls to the central star. If the packing

fraction is 10^{-3}, the size of an aggregate with St = 1 is $\simeq 1 \times 10^2$ m at 20 au. The infalling aggregates of St = 1 continue to collide with other aggregates. Further growth of the aggregates to planetesimals proceeds inside 10 au, where the infalling aggregates can concentrate (Okuzumi et al. 2012). The gravitational attraction plays a central role after the formation of planetesimals.

Figure 3 shows the required time $\tau_{\rm eq}$ to reach $T_{\rm eq}$, the time to trigger crystallization. If the formation timescale of planetesimals is considerably shorter than $\tau_{\rm eq}$, heating proceeds after the formation of planetesimals. In this case, the compaction of a planetesimal owing to self-gravity might be affected by sintering. This is because sintering greatly increases the mechanical strength of an icy dust aggregate. The resulting planetesimals have extremely low densities such as $\phi = 10^{-3}$.

If the formation timescale of planetesimals is comparable to or longer than $\tau_{\rm eq}$, the collisional evolution of icy dust aggregates would change. In this case, sintering proceeds to a large extent inside an aggregate. As shown by Equation (19), the thickness of a nonsintered zone is $\sim 10^2$ m if $\phi = 10^{-3}$. The mechanical strengths substantially increase below this zone. The collisional outcome of the sintered aggregate would be affected if the depth of penetration during a collision is larger than the thickness. In this case, the collisional sticking is difficult because the brittle disruption occurs (Sirono & Ueno 2017). As a result, the collisional outcome becomes bouncing or fragmentation. The growth of an icy aggregate stops when the penetration depth is larger than that of the sintered zone.

4.2. Amount of Impurities and Latent Heat of Crystallization

Figure 10 clearly shows that there is a critical L/L_0 to proceed sintering. Below the critical L, sintering does not proceed and the mechanical properties of an aggregate do not change. The latent heat of crystallization decreases as the content of impurities increases, because the impurities take the latent heat of sublimation and decrease L. It is important to clarify the critical content of impurities in H_2O ice. Here we investigate CO, for example. Kouchi & Sirono (2001) measured the latent heat of sublimation of CO associated with the crystallization of amorphous H_2O ice as $L_{\rm CO} \simeq 6.9 \times 10^{-20}$ J. Suppose that a fraction x of amorphous H_2O ice is replaced by CO. Then the latent heat is given by $L(x) = L_0(1 - x) - xL_{\rm CO}$. If the critical latent heat is $L/L_0 = 0.4$ (Figure 10), the corresponding molar fraction of CO is $x = 0.02$, obtained by solving $L(x) = 0.4L_0$. This fraction is smaller than those around low-mass young stellar objects ($x = 0.05$; Gibb et al. 2004). Amorphous H_2O ice containing CO more than the critical fraction of $x = 0.02$ is not sintered, and even the heating of ^{26}Al proceeds to some extent. However, it should be noted that the latent heat does not change if the impurities concentrate to form pure ice.

The sublimated CO molecules diffuse to the surface of an aggregate and escape, because the condensation temperature of CO is $\simeq$19 K, which is much lower than the aggregate temperature. However, the condensation temperatures of CO_2 and NH_3 are 68 and 84 K, respectively. If these molecules are contained as impurities, the mechanical strengths of an aggregate can change owing to condensation. As shown in Figure 6 and Equation (19), the temperature is maintained low around the surface. Impurity gas diffuses to the surface and condenses when the temperature becomes lower than the condensation temperature. Because condensation proceeds exactly at the condensation temperature, a condensed region of impurities appears inside the low-temperature region. The mechanical strength increases accordingly at the condensed region. The location of the condensed region depends on the ambient temperature T_0. It should be noted that this process happens even if L is smaller than the critical value. Figure 7 displays that crystallization proceeds to a large extent even if $L < 0$. In this case, CO_2 and NH_3 condense at $r/R = 0.98$ and 0.94, respectively, for $T_0 = 50$ K. Thus, this condensation process inevitably changes the strengths of an aggregate irrespective of L.

Another important factor is the amount of ^{26}Al contained in the silicate part of grains. We assumed that the content is that when calcium-aluminium-rich inclusion (CAI) is formed. If the formation time is delayed compared to that of CAI, the ^{26}Al content decreases according to the decay of ^{26}Al. Thus, the ^{26}Al content and the corresponding $Q_{\rm Al}$ decrease. If the formation time of an aggregate is 100 Myr (decay constant of ^{26}Al) after that of CAI, $Q_{\rm Al}$ is decreased by a factor of e^{-1}. In this case, the time required to reach $T_{\rm eq}$ is prolonged by a factor of e^{-1} accordingly. Then the sintering might not occur before the formation of planetesimals.

Finally, the mass fraction of ice $\chi_{\rm ice}$ can be lowered by some heating mechanism before the formation of an aggregate. In this case, $Q_{\rm Al}$ becomes larger than that assumed in this study, and sintering proceeds in smaller aggregates than $R = 2 \times 10^2$ m obtained in this study.

5. Conclusion

We clarified whether the temperature inside a porous icy dust aggregate increases or not owing to the decay of ^{26}Al. It has been shown that the temperature increases against heat transfer mechanisms, including molecular transport and radiation. The temperature inside the aggregate increases sufficiently to trigger the crystallization of amorphous ice. During the crystallization, the temperature increases further, and sintering proceeds to grow a neck between grains. The growth of an aggregate might stop owing to sintering, depending on the formation timescale of planetesimals.

The author is thankful for the constructive comments by an anonymous reviewer. This work was supported by JSPS KAKENHI grant no. 17K05631.

References

Bauer, I., Finocchi, F., Duschl, W. J., Gail, H.-P., & Schloeder, J. P. 1997, A&A, 317, 273
Blackford, J. R. 2007, JPhD, 40, R355
Chiang, E. I., Joung, M. K., Creech-Eakman, M. J., et al. 2001, ApJ, 547, 1077
Ghormley, J. A. 1968, JChPh, 48, 503
Ghosh, A., & McSween, H. Y. 1998, Icar, 134, 187
Gibb, E. L., Whittet, D. C. B., Boogert, A. C. A., & Tielens, A. G. G. M. 2004, ApJ, 151, 35
Haruyama, J., Yamamoto, T., Mizutani, H., & Greenberg, J. M. 1993, JGR, 98 15709
Hayashi, C., Nakazawa, K., & Nakagawa, Y. 1985, in Protostars and Planets II, ed. D. C. Black & M. S. Matthews (Tucson, AZ: Univ. Arizona Press), 1100
Kataoka, A., Tanaka, H., Okuzumi, S., & Wada, K. 2013, A&A, 557, L4
Kouchi, A., Greenberg, J. M., Yamamoto, T., & Mukai, T. 1992, ApJL, 388, L73
Kouchi, A., & Sirono, S. 2001, GeoRL, 28, 827
Krause, M., Blum, J., Skorov, Yu. V., & Trieloff, M. 2011, Icar, 214, 286
Michikoshi, S., & Kokubo, E. 2016, ApJL, 825, L28
Miyake, K., & Nakagawa, Y. 1993, Icar, 106, 20
Neumann, W., Breuer, D., & Spohn, T. 2012, A&A, 543, A141

Oba, Y., Miyauchi, N., Hidaka, H., et al. 2009, ApJ, 701, 464
Oba, Y., Watanabe, N., Hama, T., et al. 2012, ApJ, 749, 67
Okuzumi, S., Tanaka, H., Kobayashi, H., & Wada, K. 2012, ApJ, 752, 106
Petrenko, V. F., & Whitworth, R. W. 2002, Physics of Ice (Oxford: Oxford Univ. Press)
Schmitt, B., Espinasse, S., Grim, R. A. J., Greenberg, J. M., & Klinger, J. 1989, in ESA Special Publication 302 Physics and Mechanics of Cometary Materials (Munster: ESA), 65
Sirono, S. 2011, ApJ, 735, 131
Sirono, S., & Ueno, H. 2017, ApJ, 841, 36
Wakita, S., & Sekiya, M. 2011, EP&S, 63, 1193